Publication Year	2016
Acceptance in OA@INAF	2020-12-16T10:34:52Z
Title	Sensitivity of net thermal flux to the abundance of trace gases in the lower atmosphere of Venus
Authors	Lee, Yeon Joo; Sagawa, Hideo; Haus, Rainer; STEFANI, STEFANIA; Imamura, Takeshi; et al.
DOI	10.1002/2016JE005087
Handle	http://hdl.handle.net/20.500.12386/28877
Journal	JOURNAL OF GEOPHYSICAL RESEARCH (PLANETS)
Number	121

AGU PUBLICATIONS

JGR

Journal of Geophysical Research: Planets

RESEARCH ARTICLE

10.1002/2016JE005087

Key Points:
- Updated CO_2 collision-induced absorption
- Considerable SO_2, H_2O and OCS influences on net thermal flux in the deep atmosphere
- Successful reproduction of the in situ net thermal flux profiles obtained from Night and North probes of Pioneer Venus using 20-50 ppmv H_2O

Supporting Information:
- Supporting Information S1

Correspondence to:
Y. J. Lee,
leeyj@ac.jaxa.jp

Citation:
Lee, Y. J., H. Sagawa, R. Haus, S. Stefani, T. Imamura, D. V. Titov, and G. Piccioni (2016), Sensitivity of net thermal flux to the abundance of trace gases in the lower atmosphere of Venus, *J. Geophys. Res. Planets*, *121*, 1737–1752, doi:10.1002/2016JE005087.

Received 25 MAY 2016
Accepted 16 AUG 2016
Accepted article online 20 AUG 2016
Published online 20 SEP 2016

Sensitivity of net thermal flux to the abundance of trace gases in the lower atmosphere of Venus

Yeon Joo Lee[1], Hideo Sagawa[2], Rainer Haus[3], Stefania Stefani[4], Takeshi Imamura[1], Dmitrij V. Titov[5], and Giuseppe Piccioni[4]

[1]ISAS/JAXA, Sagamihara, Japan, [2]Department of Astrophysics and Atmospheric Science, Faculty of Science, Kyoto Sangyo University, Kyoto, Japan, [3]Institute for Planetology, Westfälische Wilhelms-Universität Münster, Münster, Germany, [4]INAF-IAPS, Rome, Italy, [5]ESTEC/ESA, Noordwijk, Netherlands

Abstract We calculated the net thermal flux in the atmosphere of Venus from the surface to 100 km altitude. Our atmospheric model was carefully constructed especially for altitudes below the clouds (<48 km), using recent CO_2 absorption data. It includes updated collision-induced absorptions in the <250 cm^{-1}, 1200–1500 cm^{-1}, and 2650–3130 cm^{-1} wave number ranges. We studied sensitivity of the net thermal flux below the clouds on the abundances of trace gases that were varied within the range reported by observations. Our results reveal a considerable effect of trace gases on radiative budget. We successfully simulate net thermal flux profiles measured in situ by the Night and North probes of Pioneer Venus using 20–50 ppmv H_2O, suggesting that the high H_2O abundance of 200 ppmv derived in the earlier analysis is not required. Our sensitivity study shows that the trace gases SO_2, H_2O, and OCS are effective thermal agents, while CO and HCl influences are rather weak. We suggest that the influence of the former three gases should be taken into account to estimate the net radiative energy in the deep atmosphere.

1. Introduction

The outgoing thermal flux from Venus to space is about 160 W m^{-2}, which is in almost radiative balance with the absorbed solar radiation flux and corresponds to an effective temperature close to 230 K [*Schofield and Taylor*, 1982; *Moroz et al.*, 1985; *Haus et al.*, 2015a]. About 500 K difference between the 735 K surface temperature and the effective temperature indicates the presence of a strong greenhouse effect [*Seiff et al.*, 1985] caused mainly by a dense CO_2 atmosphere and the thick cloud deck [*Bullock and Grinspoon*, 2001; *Titov et al.*, 2007]. These opacity sources prevent an upward thermal flux from the lower atmosphere, and the outgoing flux corresponds to the temperature near the cloud top level. Therefore, the observed thermal emission is close to that of the 220–260 K black body radiation in the 5–50 μm range [*Titov et al.*, 2007], and it is difficult to characterize the thermal flux below the clouds through the use of remote sensing techniques.

Very small amounts of thermal energy from the deep atmosphere are leaking out through the so-called atmospheric transparency windows at several specific wavelengths such as 1.7 μm and 2.3 μm [*Allen and Crawford*, 1984]. These atmospheric window spectra have been used to analyze trace gaseous abundances below the clouds as well as cloud opacities [*Pollack et al.*, 1993; *Meadows and Crisp*, 1996; *Marcq et al.*, 2006, 2008; *Arney et al.*, 2014; *Haus et al.*, 2015b]. But these spectra at the limited range cannot be used to understand thermal energy balance at low altitudes. In situ measurements by Pioneer Venus descent probes in 1978 provided a unique opportunity to measure net flux profiles below the clouds, although an error correction was necessary due to “through-flow” effects [see *Revercomb et al.*, 1982, 1985]. The results showed that the net flux ranges from ~10 W m^{-2} to ~90 W m^{-2} near the cloud base level (40–50 km). To explain this unexpectedly low value of the observed net flux, *Revercomb et al.* [1985] suggested a large quantity of water vapor, about 5000 ppmv. This is also based on in situ measurement data from the gas chromatograph on board Pioneer Venus, which reported 0.519% H_2O concentration [*Oyama et al.*, 1980]. The gas chromatograph measurement however could have been affected by sulfuric acid cloud particles blocking inlet of the instrument and generating water by chemical reactions at the inlet surface thereby explaining the large H_2O abundance [*von Zahn et al.*, 1983]. Such a large quantity of water vapor has not been observed by subsequent experiments. Venera 9/10 measured 300 ppmv [*Marov*, 1978], and much less water vapor abundance, 26–32 ppmv, was reported using ground-based and Venus Express observations [*Marcq et al.*, 2006, 2008; *Haus et al.*, 2015b;

Arney et al., 2014]. As a consequence, the reason for the lowest net thermal flux value derived by *Revercomb et al.* [1985] is not yet understood.

On global scale, solar insolation is strongest at the equator and much smaller at high latitudes. This excess radiative energy at low latitudes should be distributed by a global circulation, a Hadley-like one that consists of ascending motion at low latitudes and descending at high latitudes. This global circulation may extend to below the clouds [*Taylor*, 2006], as an observed CO abundance reveals its horizontal distribution around 35 km altitude [*Tsang et al.*, 2009], even though solar radiance will decrease quickly below the cloud layer. The observed increasing net thermal flux toward high latitude could support this global circulation, because the observation indicates increasing radiative cooling at high latitudes and requires a downward motion to compensate radiative cooling by adiabatic heating [*Revercomb et al.*, 1985]. However, the latitudinal variation of the net thermal flux was explained with unrealistically large range of water vapor abundance, so it is difficult to be understood with the currently observed water vapor abundance, less than 50 ppmv. On the other hand, the influence of trace gases and aerosols on the thermal flux has not yet been explored enough with updated gaseous opacity data [*Snels et al.*, 2014], and hence might not have been sufficient at the time of the in situ measurements.

There are recent studies on the atmospheric radiative energy balance that encompass the lower atmosphere below the clouds [*Haus et al.*, 2015a; *Lebonnois et al.*, 2015]. *Haus et al.* [2015a] showed a possible implication of trace gases on net radiative energy balance but more focused on the cloud bottom level and above altitudes. *Lebonnois et al.* [2015] considered CO_2 collision-induced absorptions, including data of *Stefani et al.* [2013] in the 2900–3100 cm^{-1} range. Their study pointed out that atmospheric opacity in the 3–7 µm range plays an important role on the net energy balance below the clouds, and they introduced an arbitrary continuum of 2×10^{-6} $cm^{-1}amagat^{-2}$ above 3 µm in order to make balanced net energy in the deep atmosphere. In this study, we compare possible atmospheric opacity sources using the most recent gaseous absorption data (section 2), including the data of *Stefani et al.* [2013] in the 2650–3130 cm^{-1} range. We explore the influences of trace gaseous abundance on net thermal flux (section 3). The results are discussed in section 4, and the summary is in section 5.

2. Description of Calculation

We considered the broad spectral range of thermal emission ranging from 50 to 8300 cm^{-1} (=1.2–200 µm). A fast line-by-line calculation method and the Spherical Harmonic Discrete Ordinate Method (SHDOM) [*Titov and Haus*, 1997; *Evans*, 1998] were used to calculate monochromatic upward and downward flux profiles. This was described by *Lee et al.* [2015], but details in the atmospheric gaseous absorption calculation had been greatly improved from this previous study to take into account net radiative energy balance below the clouds (see section 2.2). We performed calculations with a 0.1 cm^{-1} spectral resolution.

2.1. Atmospheric Temperature and Pressure Model

Atmospheric temperature, pressure, and density profiles at low latitude were taken from the Venus International Reference Atmosphere (VIRA) [*Seiff et al.*, 1985]. Pole-to-equator temperature difference below 50 km is small, 10 K at 40 km altitude and only 3 K at 35 km [*Seiff et al.*, 1985]. The density profile of VIRA has been taken into account with care because of the imperfect gas compressibility factor (ζ) which originally comes from *Hilsenrath et al.* [1960]. We find that VIRA density above 15 km altitude agrees well with the pure CO_2 density in National Institute of Standards and Technology webbook (http://webbook.nist.gov/chemistry/fluid/), describing thermophysical properties of fluids with recent references.

2.2. Gaseous Opacity

Gaseous absorptions due to CO_2, N_2, H_2O, SO_2, OCS, HCl, CO, HF, and H_2S were included in our atmospheric model. The mixing ratio of CO_2 and N_2 was fixed to be 96.5% and 3.5%, respectively [*Seiff et al.*, 1985]. The abundance of other trace gases varied with altitude. Figure 1 shows these vertical profiles of volume mixing ratios taken from *Titov et al.* [2007] that are used as a standard in this study (hereafter "STD"). The variability of trace gases will be discussed in section 3. Figure 2a shows calculated absorption coefficients (km^{-1}) of all gases at 40 km. As shown in this figure, CO_2 absorption is dominant at all wave numbers, but other gases can also be significant opacity sources at weak CO_2 absorption ranges.

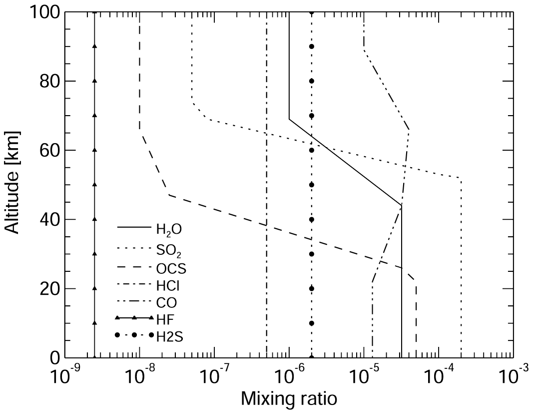

Figure 1. Vertical profiles of trace gas mixing ratios taken from *Titov et al.* [2007].

2.2.1. CO_2

CO_2 absorption makes the deep atmosphere opaque, and the net flux profiles are controlled in radiation at CO_2 windows. As a consequence, absorption in distant CO_2 wings and collision-induced absorption (CIA) are important quantities that have to be considered in net thermal flux studies. Even though such absorptions are not fully understood due to insufficient theoretical and laboratory experimental studies [*Halevy et al.*, 2009; *Snels et al.*, 2014], we tried to use available data so far.

First, we used absorption line parameters taken from the HITEMP2010 line catalog [*Rothman et al.*, 2010]. In the 4000–4400 cm^{-1} and 8000–10,300 cm^{-1} spectral ranges, another database developed by *Wattson and Rothman* [1992] and *Pollack et al.* [1993] was used.

Second, we used empirical sub-Lorentzian correction factors (so-called χ factor), which were required to reproduce observed spectra at 1.0–1.18 μm, 2.3 μm, 2.7 μm, 4.3 μm, 6–40 μm [*Winters et al.*, 1964; *Pollack et al.*, 1993; *Meadows and Crisp*, 1996; *Tonkov et al.*, 1996; *Ignatiev et al.*, 1999]. We used five different factors from the literature that were determined for certain spectral ranges. The factor taken from *Ignatiev et al.* [1999] was used in the wave number range shortward of 2000 cm^{-1}, *Winters et al.* [1964] in the 2000–2600 cm^{-1} range, *Pollack et al.* [1993] in the 2600–3800 cm^{-1} range, *Tonkov et al.* [1996] in the 3800–4700 cm^{-1} range, and *Meadows and Crisp* [1996] in the range larger than 4700 cm^{-1}. A line-cutoff value of 200 cm^{-1} was used for the CO_2 absorption calculation.

Third, we took into account CO_2 CIA. *Gruszka and Borysow* [1997] data were used in the range shortward of 250 cm^{-1} and *Baranov et al.* [2004] data in the 1200–1500 cm^{-1} range. Note that CIA studied by *Baranov et al.* [2004] is valid for the temperature range from 193 K to 360 K. We assumed that the appearance of CIA does not change at higher temperatures than the given temperature range, as its temperature dependence is weak from 294 K to 473 K [*Snels et al.*, 2014]. The same was assumed at lower temperatures. We used recent laboratory experiment data in the 2650–3130 cm^{-1} range [*Stefani et al.*, 2013]. In the atmospheric windows, CIA was suggested to explain an observed spectrum. These values could be retrieved by fitting the spectral shapes of CO_2 absorption but assumed wave number-independent "continuum" in a given window. In this study, such continuum of 3×10^{-8} ($amagat^{-2}$ cm^{-1}) was used in the 2.3 μm atmospheric window in the range

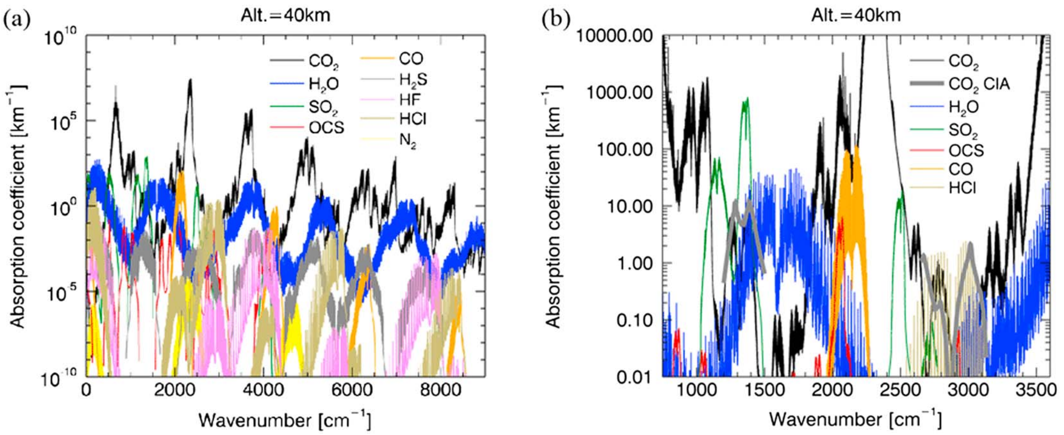

Figure 2. Absorption coefficients of all gases. This calculation uses the mixing ratio profiles shown in Figure 1 and temperature and pressure at 40 km altitude. (a) The full spectral range used in this study. (b) An enlarged area of Figure 2a in the 750–3600 cm^{-1} range and the 10^{-2}–10^{4} km^{-1} range, including CO_2 collision-induced absorption (CIA) used in this study (Table 1 and Figure 3) but excluding N_2, HF, H_2S absorptions.

Table 1. CO_2 CIA Data Sets Used in This Study

Spectral Range (cm^{-1})	CIA (Reference)
<250	*Gruszka and Borysow* [1997]
1200–1500	*Baranov et al.* [2004]
2650–2750	Equation (2) and Table S1 [*Stefani et al.*, 2013]
2750–2870	Equation (3) and Table S2 [*Stefani et al.*, 2013]
2870–3130	Equation (4) and Table S3 [*Stefani et al.*, 2013]
4000–5000	3×10^{-8} (amagat^{-2} cm^{-1}) [*Marcq et al.*, 2006]
5000–6050	7.7×10^{-9} (amagat^{-2} cm^{-1}) [*Bézard et al.*, 1990]

4000–5000 cm^{-1} [*Marcq et al.*, 2006]. It permits successful fits to an observed 2.3 μm window spectrum (section 3). A continuum value of 7.7×10^{-9} (amagat^{-2} cm^{-1}) was utilized in the 1.7 μm atmospheric window between 5000 cm^{-1} and 6050 cm^{-1} [*Bézard et al.*, 1990]. We did not use any CIA for the atmospheric windows shortward of 1.7 μm. Table 1 summarizes the CIA data sets used in this study.

We compared these data sets of CIA to the previous data measured by *Moskalenko et al.* [1979], which has been used in other Venus studies [*Bullock and Grinspoon*, 2001; *Eymet et al.*, 2009; *Takagi et al.*, 2010; *Lee and Richardson*, 2011; *Mendonça et al.*, 2015]. This comparison was done at the 1 bar pressure (0.9869 atm) and several temperatures as shown in Figure 3. There are considerable differences between the curves. For example, in the spectral range 1100–1600 cm^{-1}, CIA described by *Moskalenko et al.* [1979] has broader and stronger absorption than the observed data by *Baranov et al.* [2004] (Figure 3b). The similar behavior is observed for the CIA in the 0–450 cm^{-1} and 2570–3200 cm^{-1} ranges (Figures 3a and 3c). In addition, temperature dependences are not consistent. We decided to use the data sets of Table 1 and not to extrapolate CIA absorption at shorter or longer wave numbers than the specified ranges (e.g., as noted in *Gruszka and Borysow* [1997] for the CIA at the 0–250 cm^{-1} range).

Among these CIA data sets, data in the 2650–3130 cm^{-1} range have 1 order of magnitude weaker absorption than those in the 0–250 cm^{-1} and 1200–1500 cm^{-1} ranges (Figure 3). Nevertheless, this CIA turned out to be a significant factor in thermal flux calculation due to the high temperature of the deep atmosphere. We carefully investigated this specific CIA using the recent measurement data [*Stefani et al.*, 2013]. We divided the spectral range into three subranges, 2650–2750 cm^{-1}, 2750–2870 cm^{-1}, and 2870–3130 cm^{-1}, and then compared spectral features and CO_2 density dependence. Band integrated intensities (A) are calculated as

$$A_{\nu_1-\nu_2} = \int_{\nu_1}^{\nu_2} k_\nu \mathrm{d}\nu, \tag{1}$$

where k_ν is an absorption coefficient (cm^{-1}), and ν_1 and ν_2 are limits of a wave number range (cm^{-1}). We evaluated the CO_2 density square dependences of A, which is the characteristic feature of CIA [*Frommhold*, 1993]. A linear regression was applied to find a coefficient α (cm^4 mol^{-2}), satisfying $A = \alpha \times \rho^2$, where ρ is number density (mol cm^{-3}), as shown in Figures 4a–4c. The result in the 2650–2750 cm^{-1} range is derived as

$$A_{2650-2750} = 7.53 \times 10^4 \rho^2. \tag{2}$$

Data points in Figure 4a are corresponding to each spectrum shown in Figure 4b. The correlation coefficient of the linear fit is 0.996. We compared its spectral feature with a previous study, *Moskalenko et al.* [1979], as shown in Figure 3c and found that the shape and the peak location of the absorption coefficient of *Stefani et al.*, 2013 is different from that of *Moskalenko et al.*, 1979 especially at 2670 cm^{-1}.

The result in the 2870–3130 cm^{-1} range is derived as

$$A_{2870-3130} = 1.334 \times 10^5 \rho^2. \tag{3}$$

This coefficient is a little smaller than that retrieved by *Thomas and Linevsky* [1989]: 1.59×10^5. Measured spectra shown in Figure 4f are used in Figure 4e. The correlation coefficient of the linear fit in Figure 4e is 0.986. Its weak temperature dependence is consistent with previous studies [*Thomas and Linevsky*, 1989; *Snels et al.*, 2014].

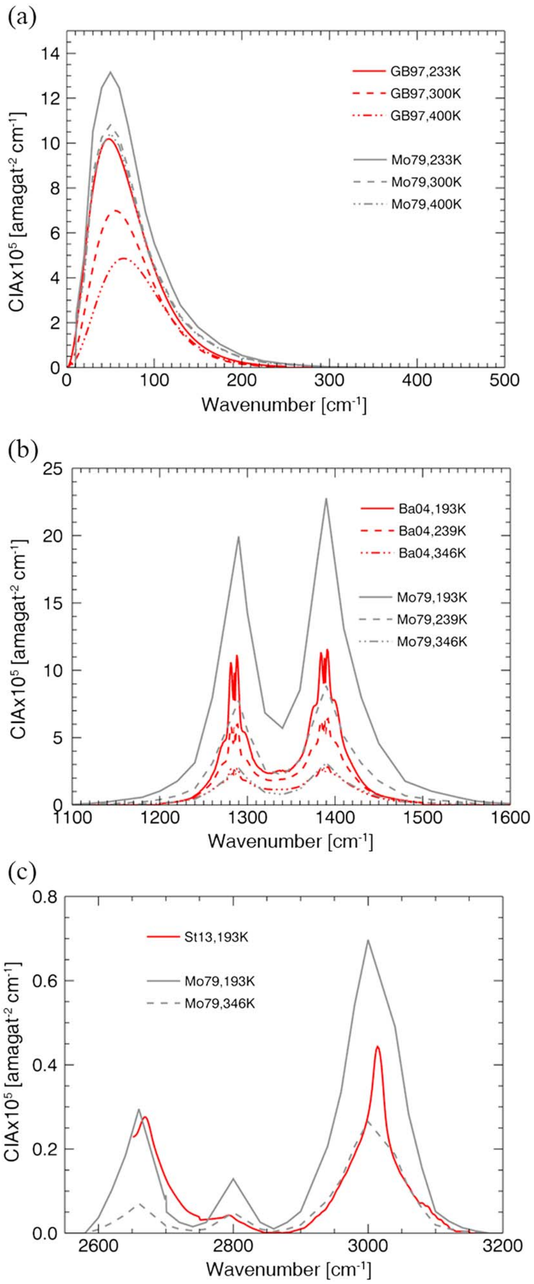

Figure 3. Comparisons of CO_2 CIA coefficients between recent data and previous data. (a) *Gruszka and Borysow* [1997] ("GB97") and *Moskalenko et al.* [1979] ("Mo79") from 0 to 500 cm^{-1}, (b) *Baranov et al.* [2004] ("Ba04") and Mo79 from 1100 to 1600 cm^{-1}, and (c) *Stefani et al.* [2013] ("St13") and Mo79 from 2550 to 3200 cm^{-1}.

There is an ambiguous CIA in the 2750–2870 cm^{-1} range. Previous studies suggested its existence [*Moskalenko et al.*, 1979; *Thomas and Linevsky*, 1989], but it is difficult to evaluate this absorption, since this possible CIA is a part of an allowed CO_2 absorption band. Three spectra among six measurements show its feature (Figure 4d). Even though the statistic reliability is low, we used these spectra to estimate this CIA in the same manner as done for the above two subranges, under the assumption of weak temperature dependence.

$$A_{2750-2870} = 1.36 \times 10^4 \rho^2. \quad (4)$$

This possible CIA is not significant due to the overlapped CO_2 band. The net thermal flux reduction caused by this CIA is less than 1.5 W m^{-2} below 40 km altitude.

For our model calculation, we used smoothed absorption coefficient spectra of the measurements (Tables S1–S3 shown in the supporting information file). The density square dependence of absorption was calculated according to equations (2)–(4). Simulated spectra are compared to the measurements in Figures 4b, 4d, and 4f, showing reasonable fits.

In the next step, we compared CIA influences on the wave number-integrated net thermal flux profiles (Figure 5). The abundance of trace gases were fixed to the STD condition. The strongest effect is caused by CIA in the 2650–3130 cm^{-1} range, since there is no other overlapped gaseous absorption (Figure 2b), and it is where strong thermal flux is emitted due to high temperature in the deep atmosphere. The continuum effect is the next strongest one. CIA in the 1200–1500 cm^{-1} range and shortward of 250 cm^{-1} are not as effective as the others, although actual absorption is strong. The CIA shortward of 250 cm^{-1} is even negligible, because of overlapped water vapor absorption (Figure 2a). Figure 5 shows that CIA affects thermal flux below the clouds but only very weakly above.

2.2.2. H_2O

We prepared two data sets for H_2O absorption. The first one is based on HITRAN2012 [*Rothman et al.*, 2013]. The air-broadened half width was multiplied by 1.7 to take into account CO_2 broadening [*Fedorova et al.*, 2008] with a line-cutoff value of 100 cm^{-1} and assumed $\chi = 1$. The second set includes laboratory experimental continuum results obtained from measurements in the 2000–9000 cm^{-1} range that were performed by the UK-based Continuum Absorption at Visible and Infrared wavelengths and its Atmospheric Relevance (CAVIAR) consortium [*Ptashnik et al.*, 2011, 2012] and at the V.E. Zuev Institute of Atmospheric Optics, Russia [*Ptashnik et al.*, 2013]. They compared the measurements between their data and another most broadly used H_2O continuum data, the Clough-Kneizys-Davies (CKD) model, the latest version Mlawer-Tobin-Clough-Kneizys-Davies (MT_CKD) model [*Clough et al.*, 2005], and showed that their measured data exhibit stronger absorption than MT_CKD.

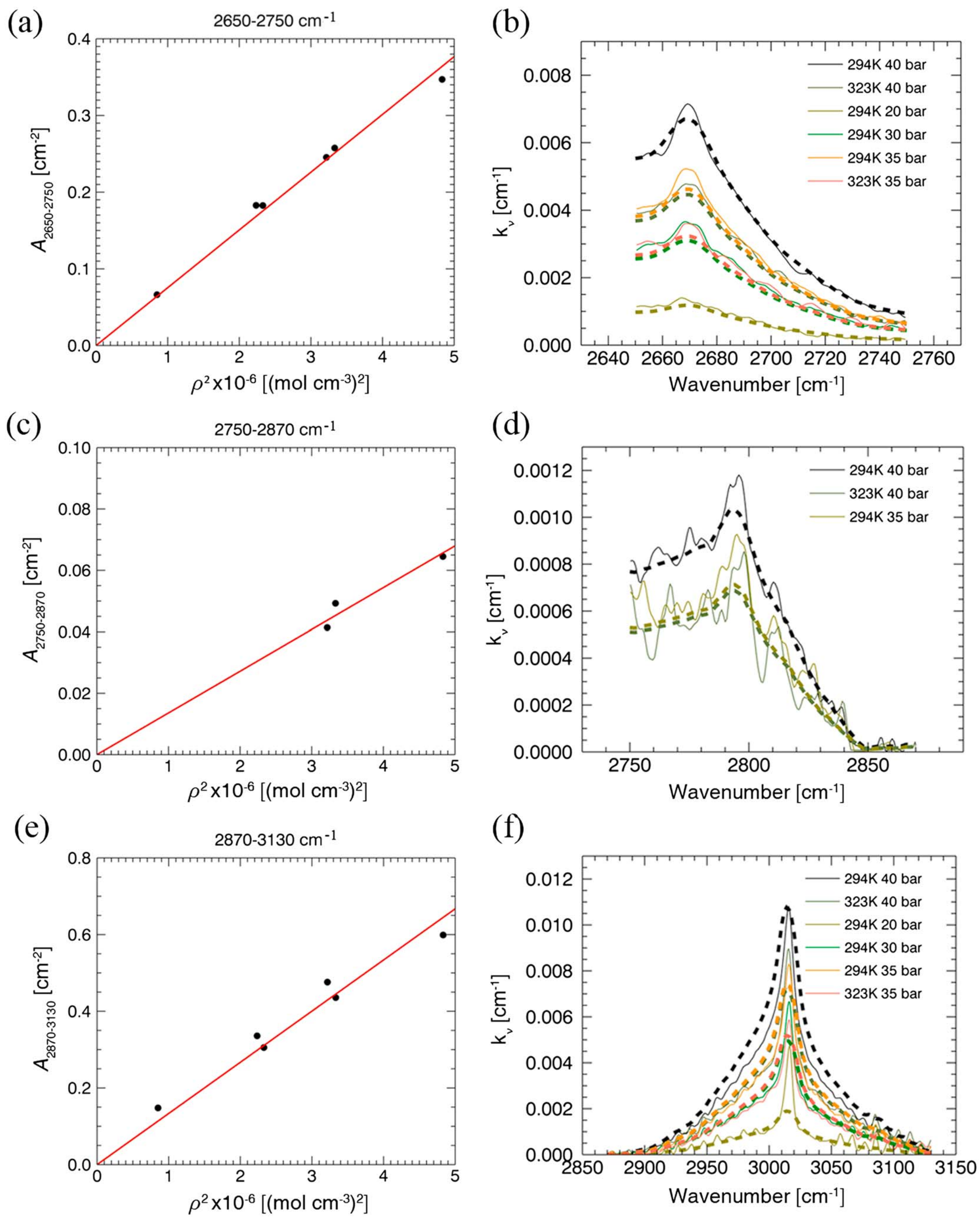

Figure 4. CO_2 CIA from laboratory experiments [*Stefani et al.*, 2013]. (a, c, and e) Band integrated intensities as a function of density square. Linear fits are shown as red solid lines. (b, d, and f) The measured absorption coefficients at different pressures and temperatures (solid lines) and input data in our model calculation (dashed lines).

We compared our first and second data sets and found that the difference is negligible, because of the relatively low abundance of H_2O. Nevertheless, we used the first data set in the 50–2000 cm^{-1} range and the second one in the 2000–9000 cm^{-1} range, since this later one is based on recent experimental measurement, meaning that this may have more appropriate absorption spectrum features than the former. For the second data set, we used UCL08 line parameter, which is a compilation of HITRAN2008 and University College London data, containing 1.5 million lines [*Shillings et al.*, 2011]. We calculated allowed absorptions as described by *Ptashnik et al.* [2012]. Then, optical depth of H_2O absorption (τ) was calculated as the sum of allowed absorption (τ_{line}) and continuum (τ_{cont}). The continuum was divided into self-continuum (C_s) and foreign continuum (C_f), as shown in the equation below,

$$\tau_{\text{cont}}(\nu,T) = C_s(\nu,T)\rho_{H_2O}P_{H_2O} + C_f(\nu,T_0)\rho_{H_2O}(P_{\text{air}} - P_{H_2O}), \tag{5}$$

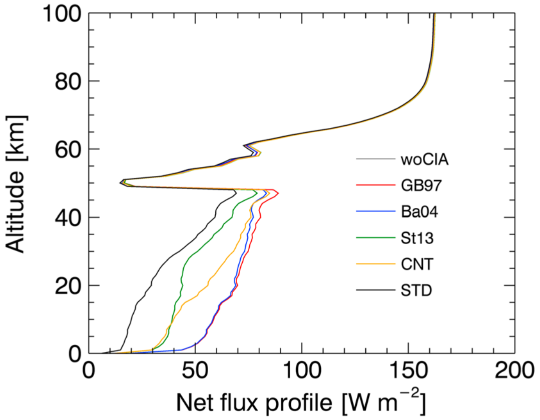

Figure 5. Influence of CO_2 CIA on the net thermal flux. Grunszka and Borysow (1997) data have been used in the 0–250 cm^{-1} range (red line, “GB97”), Baranov et al. (2004) in the 1200–1450 cm^{-1} range (blue, “Ba04”), the laboratory experimental data [*Stefani et al.*, 2013] in the 2650–3130 cm^{-1} range (green, Figure 4, “St13”), and atmospheric window continua in the 4000–6050 cm^{-1} range (yellow, “CNT”). All of CIA are used for STD (black). Without CIA (grey, “woCIA”) is almost identical to the red curve below the clouds and to the yellow curve above the clouds.

where C_s and C_f are cross-section (cm^{-2} molecule^{-1} atm^{-1}), ρ_{H_2O} is a number density of water vapor (molecule cm^{-3}), P_{air} is the total atmospheric pressure (atm), P_{H_2O} is a partial pressure of water vapor (atm), T is temperature (K), and T_0 is 400 K. C_f was measured for the Earth atmosphere and is assumed to be similar to that in the CO_2 atmosphere.

Figure 6 shows spectra of C_s and C_f. The measured C_s varies from 289 K to 472 K [*Ptashnik et al.*, 2011, 2013]. We interpolated $C_s(\nu, T)$ from 250 K to 500 K but fixed to the value at T=250 K when T is lower than 250 K or that at T=500 K when T is higher than 500 K. C_f has a weak temperature dependence, so we used the data at T=400 K [*Ptashnik et al.*, 2012].

2.2.3. Other Gases

Other trace gas line parameters were taken from the HITRAN2012 (SO_2, OCS, CO, HCl, HF, H_2S, and N_2). We used the air-broadened half width for the CO_2 broadening, a line-cutoff value of 100 cm^{-1}, and χ=1. More accurate calculation would be possible when absorption line parameters of these gases in the dense CO_2 atmosphere are available.

2.3. Cloud Models

The clouds of Venus are located between ∼48 km and ∼70 km altitudes above the surface. Many previous studies used various cloud models depending on spectral ranges and analysis methods [*Crisp*, 1986; *Pollack et al.*, 1993; *Zasova et al.*, 2007; *Ignatiev et al.*, 2009; *Haus et al.*, 2015a; *Lee et al.*, 2015]. We compared three among them, selecting Table 2 of *Crisp* [1986] (Crcld), Table 1 of *Haus et al.* [2015a] (Hacld), and a cloud model from *Lee et al.* [2015] with the aerosol scale height of 4 km and the cloud top altitude of 67 km, defined by a unity optical depth at 5 μm(ZLcld). Crcld was based on Pioneer Venus' in situ and remote sensing data. It considers lower haze from 30 km to the cloud base at 48 km. Hacld was developed to fit observed spectra at broad spectral ranges (300–1700 cm^{-1}, 2000–2800 cm^{-1}, and 4000-4600 cm^{-1}) that were measured by spectrometers onboard Venera-15 and Venus Express. ZLcld is a combination of the upper cloud model, which was used to retrieve cloud top altitudes and aerosol scale heights using a joint analysis of spectrometer and radio occultation measurement on board Venus Express and the middle and lower cloud model taken from

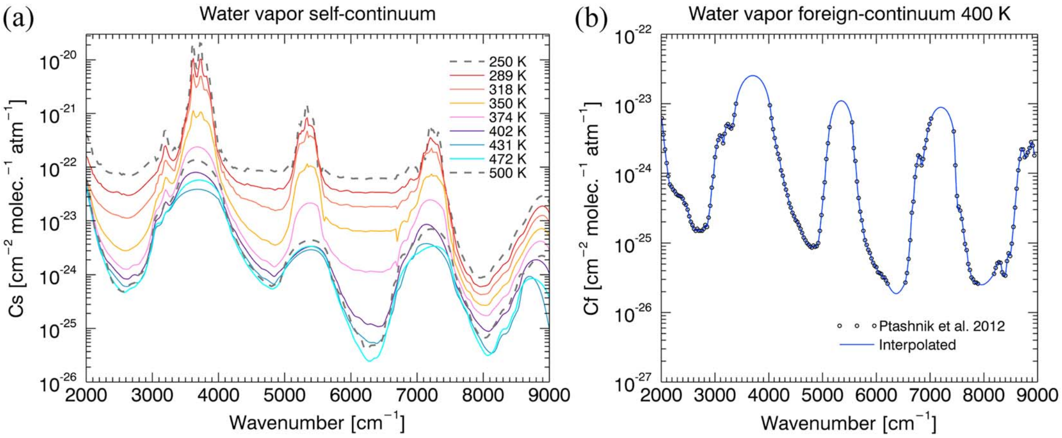

Figure 6. H_2O continua data taken from *Ptashnik et al.* [2011, 2012, 2013].

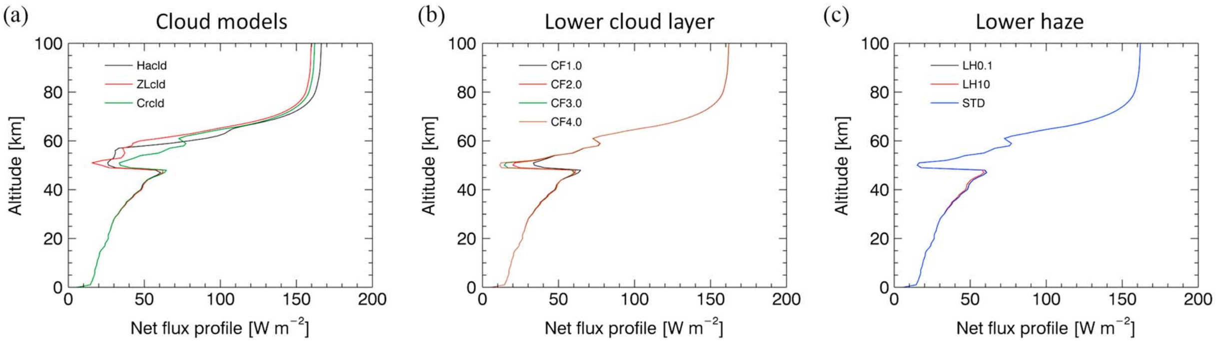

Figure 7. Influence of the aerosols on the net thermal flux. (a) Different cloud models, (b) various lower cloud opacities at 48–50 km, and (c) various lower haze opacities at 30–48 km. The three clouds were taken from *Haus et al.* [2015a] ("Hacld"), *Lee et al.* [2015] ("ZLcld"), and *Crisp* [1986] ("Crcld"). The opacity of the lower clouds is increased by a factor of 1 to 4 (CF1.0–CF4.0) in Figure 7b. The opacity of the lower haze is changed to 1 order of magnitude higher (LH10) or lower (LH0.1) in Figure 7c.

Zasova et al. [2007], which is based on Pioneer Venus and Venera data. Since each of these cloud models has been developed for different purposes, we assumed that the differences between them may be representative to characterize the possible range of cloud structure variations. Four-mode size distributions of 75% sulfuric acid aerosols were used for all three models: mode 1 – $\bar{r} = 0.15$µm and $\sigma = 1.91$, mode 2 – $\bar{r} = 1.05$µm and $\sigma = 1.21$, mode 2′ – $\bar{r} = 1.40$µm and $\sigma = 1.23$, and mode 3 – $\bar{r} = 3.85$µm and $\sigma = 1.30$, where $\bar{r}$ is a mean radius and σ is a standard deviation for a lognormal size distribution [*Pollack et al.*, 1980a]. The optical properties of aerosols were calculated using Mie code calculation [*Palmer and Williams*, 1975; *Wiscombe*, 1980] (N. Ignatiev, personal communication, 2010).

Figure 7a illustrates net thermal fluxes obtained for the three cloud models. The net fluxes below the clouds are very similar. Thus, the cloud structure has a negligible influence on the net thermal flux below the clouds. Above the clouds, the net flux varies, but this is a reasonable result considering different cloud top altitudes and structures (e.g., Hacld: 71.3 km at 1 µm, Crcld: ~71 km at 0.63 µm, and ZLcld: 67 km at 5 µm). These changes in cloud parameters affect the upward directed flux up to the top of the atmosphere. Then, we changed the lower cloud opacity of Crcld (48–50 km) by increasing the cloud number density up to a factor of 4 in the same manner as done by *Arney et al.* [2014]. The corresponding results shown in Figure 7b confirm the weak influence of the lower cloud opacity on the net thermal flux below the clouds. There is no effect on the outgoing thermal flux at altitudes higher than about 55 km because of unaffected cloud top altitudes. Finally, we changed only the lower haze opacity in the 30–48 km altitude range; increasing or decreasing it by 1 order of magnitude (Figure 7c). The result reveals the weak influence of the lower haze on the net thermal flux below the clouds due to too small size of haze particles compared to the maximum wavelength of thermal emission below the clouds.

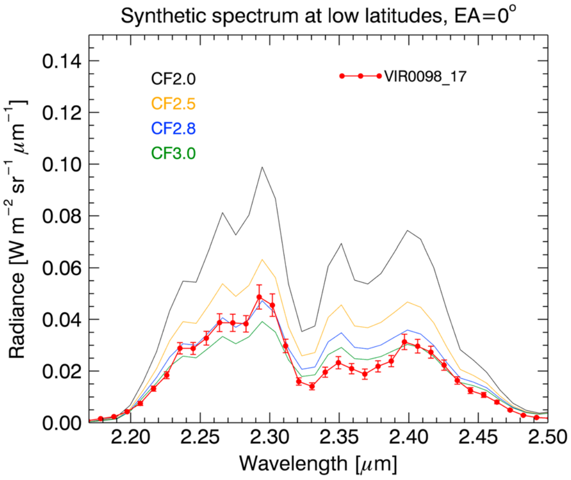

Figure 8. Comparison between synthetic spectra and an observed spectrum at the 2.3 µm atmospheric window. The observation is taken from VIRTIS-M-IR on board Venus Express (orbit #0098 and qube #17). The observed spectrum is an average at low latitudes with less than 5° emission angle at night side.

2.4. Comparison With Observation

We compared our synthetic radiances with an observed 2.3 µm window spectrum to validate our model calculation and also to determine a reasonable opacity of the lower cloud layer. Figure 8 shows this result. The synthetic spectra were calculated at 0° emission angle using different lower cloud opacities ranging from a factor of 2 (CF2.0) to a factor of 3 (CF3.0). The observed spectrum is an average of 370 spectra, having the same condition of emission angles (<5°) at 33° (±2°)S latitude and around 21 h local time measured by the Visible and Infrared Thermal Imaging Spectrometer (VIRTIS)/Venus Express [*Piccioni et al.*, 2006]. The result shows that the synthetic spectrum for CF2.8 fits the observation well in the 2.2–2.3 μm range that is almost not influenced by trace gas variations as it is the case in the 2.3–2.5 μm range. It is important to note that an observed radiance at this atmospheric window may strongly vary with local time and latitude. This implies a high variability of the lower cloud opacity, for example, from CF1.0 to CF3.0 [*Arney et al.*, 2014]. However, our interest is more directed to the net thermal flux below the clouds, where the dependence on the clouds is weak (see Figure 7). For our study, any CF is acceptable between CF1.0 and CF4.0, corresponding to a total cloud opacity from 29 to 46 as calculated at 1 μm. This range of cloud opacities is close to the observed variation range from VIRTIS that shows 33–51 [*Haus et al.*, 2015b]. We decided to use CF2.8 of Crcld as STD because of the good fitting shown in Figure 8. The variation of CF alters the thermal heating at the cloud bottom level. This would affect the cloud level convection [*Baker et al.*, 1998; *Imamura et al.*, 2014] and could be investigated in a future study.

Measured and synthetic spectra in the 2.3–2.5 μm range depend on the abundance of trace gases, such as CO, H_2O, OCS, and SO_2 [*Marcq et al.*, 2008; *Arney et al.*, 2014; *Haus et al.*, 2015b]. Differences between synthetic and observed spectra can be reduced by changing the abundance of the trace gases from STD, but this is not the scope of the present study.

3. Results

We investigated the sensitivity of the net thermal flux in the lower atmosphere of Venus to trace gas abundances of SO_2, H_2O, OCS, CO, and HCl. Spectral-integrated net flux profiles are compared, while the abundances of each trace gas was varied below 52 km altitude and all the others were fixed to STD (Figure 1). In order to understand effective spectral range and altitude, spectral sensitivity to an abundance of a gas is also studied, $-\mathrm{d}F_{\mathrm{net},\nu}(A_{\mathrm{gas}}, z)/\mathrm{d}A_{\mathrm{gas}}$, where $F_{\mathrm{net},\nu}$ is a monochromatic net thermal flux (W/(m^2 cm^{-1})), A_{gas} is an abundance of a gas, ν is a wave number, and z is an altitude. Possible vertical gradients of trace gases were ignored in this sensitivity study, except for STD.

3.1. SO_2

Previous studies reported the abundance of SO_2 as 126–185 ppmv with deviations from ±40 to ±70 ppmv using in situ measurement and the 2.3 μm atmospheric window observation which corresponds to around 35 km altitude [*Oyama et al.*, 1980; *Pollack et al.*, 1993; *Marcq et al.*, 2008]. The most recent ground-based observation at the 2.3 μm wavelength reported considerable spatial variability from 0 to 260 ppmv [*Arney et al.*, 2014]. Their high spectral resolution data with $R = 3500$ is sufficient to retrieve SO_2 abundance from the narrow absorption range at 2.45–2.48 μm. Vertical distributions of SO_2 abundance were measured in situ by ISAV1 and ISAV2 on board Vega balloons. The results showed a decreasing trend of the SO_2 abundance downward in altitude, from 125–140 ppmv at 42 km to 20–25 ppmv at 12 km altitude [*Bertaux et al.*, 1996]. The observed abundance of SO_2 in the lower atmosphere triggered discussions on chemical process. For example, *Fegley and Treiman* [1992] suggested the losing process of SO_2 through the reaction between SO_2 and $CaCO_3$ (atmosphere-surface interaction) and showed their model result of significantly low SO_2 abundance, less than 10 ppmv below ∼15 km. The atmosphere-surface interaction, however, may be a localized process [*Krasnopolsky*, 2007], and volcanism may be a sufficient source [*Fegley and Treiman*, 1992]. Therefore, the range of SO_2 abundance variation is not fully understood below the clouds. In this study, we take into account a SO_2 mixing ratio variability in the range of 0–300 ppmv. But we note that the zero abundance would be extreme.

Figures 9a and 9b show the results. A significant increase of the net flux appears when we use 0 ppmv. The net flux increases by ∼60 W m^{-2} compared to that using 300 ppmv. More than 20 ppmv mixing ratio can produce sufficient opacity to suppress this increase, and the change of the net flux becomes rather small from 50 to 300 ppmv (5 W m^{-2}). The SO_2 absorption bands are not as broad as those of H_2O and CO_2. But as shown in Figure 9b, the largest net flux variation happens in the 1100–1200 cm^{-1} range, which accommodates a strong SO_2 absorption band. On the other hand, this spectral range is characterized by comparatively small opacities of other gases including CO_2 (cf. Figure 2b). Therefore, if the abundance of SO_2 is not high enough (<20 ppmv) in the lower atmosphere, then this atmospheric window can enable effective thermal cooling below the clouds. However, the variations of SO_2 abundance below the clouds do not affect net flux within and above the clouds. The difference between the net flux profiles decreases quickly below 30 km altitude because of pressure broadening of CO_2 absorption that effectively “closes” the spectral window.

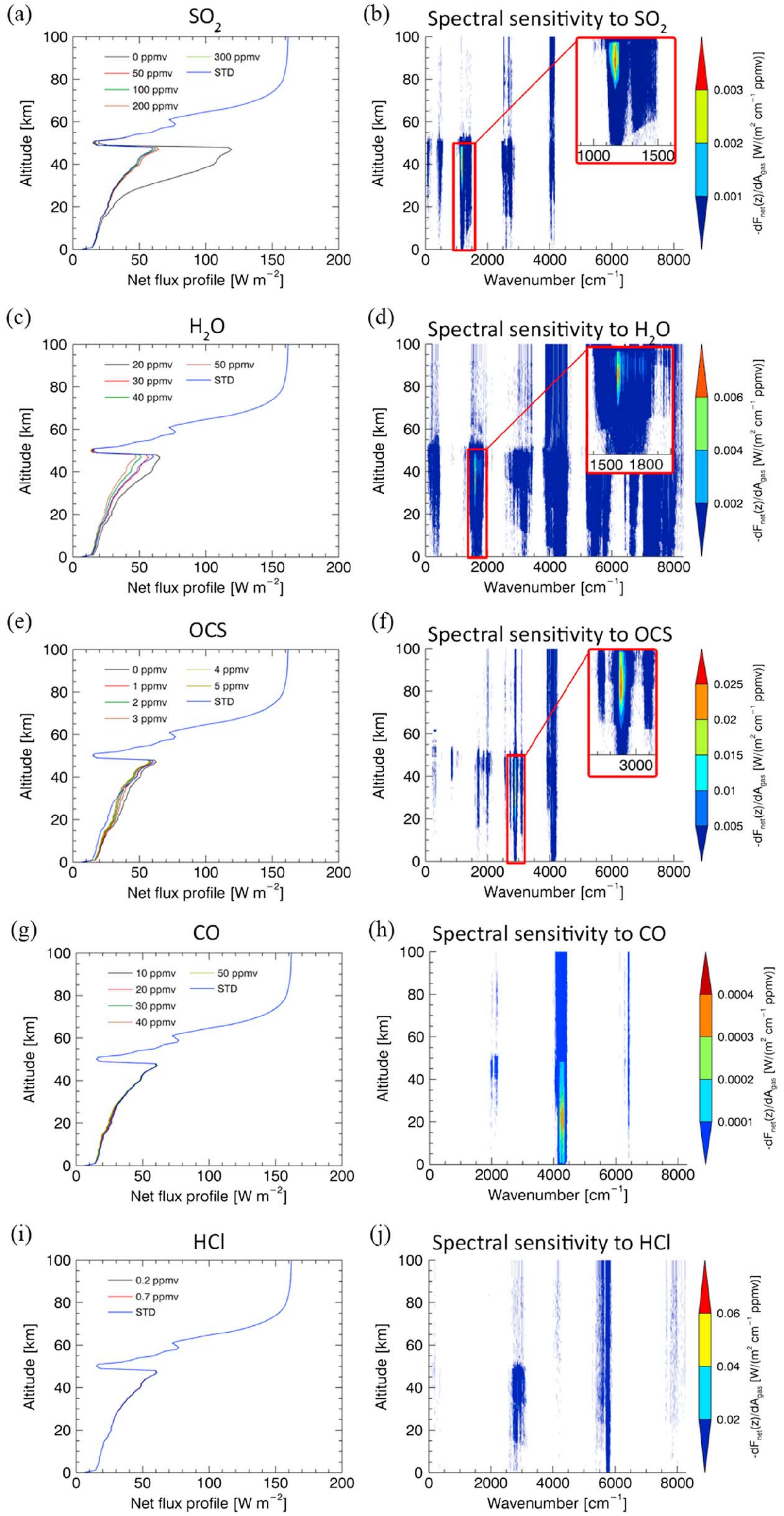

Figure 9. Sensitivity of the net thermal flux to the abundance of trace gases. (a and b) The sensitivity to the SO_2 mixing ratio for the wave number-integrated net flux profiles and for the monochromatic net flux profile between minimum (0 ppmv) and maximum (300 ppmv), respectively. (c and d) The same as Figures 9a and 9b but for the 20–50 ppmv of H_2O. (e and f) The same but for the 0–5 ppmv of OCS. Figures 9b, 9d, and 9f have enlarged boxes, showing most sensitive spectral regions of each gas between 0 and 50 km. (g and h) The same but for the 10–50 ppmv of CO. (i and j) The same but for the 0.2–0.7 ppmv of HCl.

Table 2. Summary of the Sensitivities of the Net Thermal Flux to the Abundance of Trace Gases Below the Clouds

Gas	SO_2	H_2O^a	OCS^a	CO^a	HCl
Min (ppmv)	$0^b(80)$	20	0	10	0.2
Max (ppmv)	300	50	5	50	0.7
$\Delta F_{net} = F_{net}(\min) - F_{net}(\max)$					
Max ΔF_{net} (W m^{-2})	59.9 (3.1)	20.0	6.4	2.2	0.5
Altitude of max ΔF_{net} (km)	≥43 (≥47)	43	32–33	21–22	36–38
Most affected spectral	1100–1200	∼1600	∼2900	4150–4350	∼2900
Region (cm^{-1})	(∼440–450, 1200–1230)				

[a] A vertical gradient of abundance is ignored.
[b] Extreme case. Minimum 80 ppmv case is shown in parentheses.

3.2. H_2O

We consider an abundance range of H_2O from the previous observations between 20 and 50 ppmv [*Bézard et al.*, 1990; *Pollack et al.*, 1993; *Bézard et al.*, 2009; *Marcq et al.*, 2008; *Arney et al.*, 2014; *Haus et al.*, 2015b]. The much larger abundance of H_2O, 150–300 ppmv, which was reported by Venera [*von Zahn et al.*, 1983], is not considered in this study, because this has not been confirmed by other observations.

As shown in Figures 9c and 9d, the net thermal flux profile near 40 km decreases by ∼20 W m^{-2}, when the mixing ratio of H_2O increases from 20 to 50 ppmv. This is the second strongest influence on net flux after that of SO_2, but the variation ranges of mixing ratio is much smaller than that of SO_2. The H_2O absorption extends over broad spectral range and higher H_2O abundances can reduce the net thermal flux very effectively. The spectral sensitivity is the strongest around 1600 cm^{-1}, where H_2O opacity is dominant (Figures 2 and 9d).

3.3. OCS

We compare thermal flux profiles for abundance variations of OCS from 0 and 5 ppmv assuming a constant profile below 52 km. Previous observations at the 2.3 μm atmospheric window reported an increasing OCS abundance below 30 km [*Pollack et al.*, 1993; *Marcq et al.*, 2005]. Also, there are considerable differences in observed abundance above 30 km ranging from less than 1 ppmv to 4.4 ppmv [*Pollack et al.*, 1993; *Marcq et al.*, 2005; *Arney et al.*, 2014; *Haus et al.*, 2015b]. This may indicate possible different vertical gradients, but we simplified our sensitivity study using a constant value. A vertically varying OCS mixing ratio has been assumed for STD according to Figure 1, 0.025 ppmv at 48 km to 32 ppmv at 27 km (∼4 ppmv at 33 km). A comparison of results using STD model and a constant mixing ratio can provide a rough assessment of the influence of the vertical gradient. Figure 9e shows that the STD flux profile intersects with that of 4 ppmv constant value at ∼33 km, implying that both agree above 30 km. However, below 30 km, the STD flux profile shows the smallest value, which is caused by the large abundance of OCS. Therefore, we restrict the OCS sensitivity analysis for the altitudes above 30 km.

Figure 9e shows that the net thermal flux variation due to OCS is from 35 W m^{-2} (5 ppmv) to 42 W m^{-2} (0 ppmv) at 33 km. This is the third strongest influence on the net thermal flux changes, after those of SO_2 and H_2O. Taking into account its small range of mixing ratio variation, the sensitivity of the net thermal flux to abundance changes of OCS is relatively high compared to SO_2 and H_2O. Most effective absorption is located around 2900 cm^{-1} (Figure 9f), where CO_2 and H_2O absorptions are relatively weak. Note that the net flux change is reduced by CO_2 CIA (cf. Figure 4f).

3.4. CO and HCl

We change the abundance of CO from 10 to 45 ppmv, as reported by previous observations [*Bézard et al.*, 1990; *Pollack et al.*, 1993; *Marcq et al.*, 2008; *Tsang et al.*, 2009; *Arney et al.*, 2014; *Haus et al.*, 2015b]. A constant profile has been used below 52 km. Figures 9g and 9h show that the strongest CO influence occurs at the 2.3 μm window around 20 km, but the overall effect is rather weak.

The mixing ratio of HCl ranges from 0.2 to 0.7 ppmv [*Bézard et al.*, 1990; *Iwagami et al.*, 2008; *Arney et al.*, 2014]. This produces negligible effect on the net thermal flux (Figure 9i). Figure 9j shows that spectral ranges of high sensitivity are around 3000 cm^{-1} and 6000 cm^{-1}, where HCl absorption bands exist.

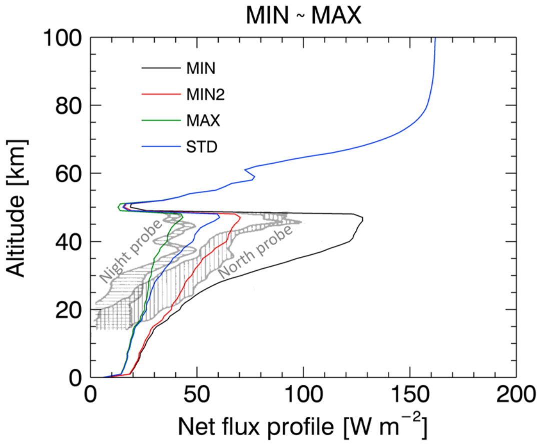

Figure 10. Comparison of net thermal flux profiles. The minimum abundance of trace gases (MIN, black), the same as MIN except for a moderated SO_2 abundance (MIN2, red), and the maximum abundance of trace gases (MAX, green) are used to calculate the net thermal flux profiles. STD is the result using Figure 1. See text for details. In situ measurement data from the North and Night probes of Pioneer Venus are also shown (grey shaded lines) [*Revercomb et al.*, 1985].

3.5. The Range of Net Flux Variations

The sensitivities of the net thermal flux to abundance variations of trace gases are summarized in Table 2. Considerable net flux variations can be caused by abundance changes of SO_2, H_2O, and OCS below the clouds, while there are weak variations due to CO abundance and negligible flux response to the abundance changes of HCl. Our results are consistent with previous studies by *Pollack et al.* [1980b] and *Tomasko* [1983] who also described H_2O and SO_2 as important thermal opacity sources. Our conclusion about the strongest influence of SO_2 is different from the previous study by *Taylor and Grinspoon* [2009]. This is caused by the different CO_2 absorption consideration, which will be discussed in more detail in section 4. The weak influence of CO and negligible effect of HCl in our result are consistent with previous studies [*Pollack et al.*, 1980b; *Tomasko*, 1983; *Titov et al.*, 2007; *Taylor and Grinspoon*, 2009].

We also compare the minimum (MIN) and maximum (MAX) abundances of all gases in order to explore the range of possible net thermal flux variations. MIN and MAX are considered as the abundances shown in Table 2 for SO_2, H_2O, OCS, and CO. MIN2 uses the same mixing ratios as MIN, except a moderate SO_2 by 80 ppmv. All gaseous abundances are constant below 52 km altitude. Figure 10 shows the result. The net thermal flux at 45 km altitude is 40 W m^{-2} for MAX and increases up to 68 W m^{-2} for MIN2 and 97 W m^{-2} for the extreme case MIN, respectively. We also investigated net flux changes due to temperature profile variations from equator to polar latitudes according to VIRA using STD abundance conditions. The difference in net flux due to the thermal structure is less than 9.7 W m^{-2} (not graphically shown here). This implies that the abundance of trace gases plays an important role in controlling the net thermal energy below the clouds, more than the meridional variation of thermal structure does.

4. Discussion

There is only one in situ observation available to compare with our calculation results. This is the data obtained by the net flux radiometers on board Pioneer Venus small probes. Among three probes the Night and North probes descended on the nightside, meaning they measured only thermal flux [*Suomi et al.*, 1980]. The primary results revealed ~50–110 W m^{-2} at the 40–50 km altitude range [*Suomi et al.*, 1980], but these values were corrected later on to 30–100 W m^{-2} by the error removal procedure [*Revercomb et al.*, 1982]. The corrected data below 48 km are compared with our results in Figure 10. This comparison shows that the variation of observed thermal fluxes below the clouds is consistent with our model calculations using various abundances of trace gases.

We find that 50 ppmv water vapor and abundances of other trace gases within their observed ranges produce enough thermal opacity to fit the measured net fluxes of the Night probe. Thus, it is not necessary to assume 100–200 ppmv water vapor as done by *Revercomb et al.* [1985]. Below 30 km altitude, the observed net thermal fluxes are smaller than our results. We identified a possible cause resulting from the error correction process applied by *Revercomb et al.* [1982]. The error term is the largest at 14 km altitude and decreases upward reaching minimum near 55 km. This error depends on the simulated net thermal flux at 14 km, since an absolute error could not be calculated. Revercomb et al. assumed 0–16 W m^{-2}, which is smaller than our calculation (20–29 W m^{-2}). Therefore, the comparison between corrected observation and our model calculation is more plausible in the 35–48 km altitude range than at lower altitudes.

Concerning the contributions of water vapor to the thermal opacities, our result is consistent with the previous studies; H_2O is an effective factor on the net flux variation [*Pollack et al.*, 1980b; *Tomasko*, 1983;

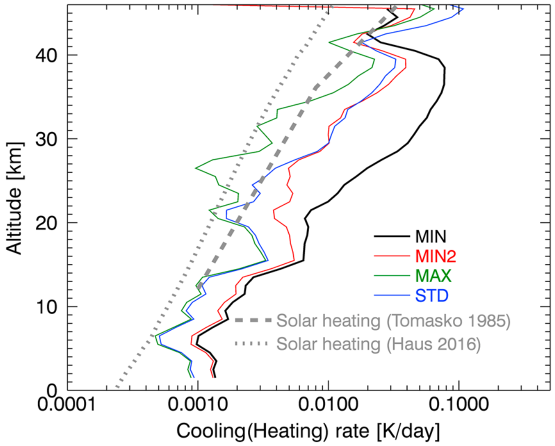

Figure 11. Comparison of cooling rate profiles. The net thermal flux profiles shown in Figure 10 are used. The global mean solar heating rate profiles are taken from *Tomasko et al.* [1985] (grey dashed line) and *Haus et al.* [2016] (grey dotted line).

Revercomb et al., 1985; *Titov et al.*, 2007; *Taylor and Grinspoon*, 2009]. SO_2 can enhance thermal cooling most significantly in this study but only for the case of less than 20 ppmv mixing ratio. This is an interesting result considering the atmospheric evolution of Venus, as *Taylor and Grinspoon* [2009] seem to underestimate the influence of SO_2, due to the used CO_2 CIA around 1100–1200 cm^{-1}. These data described by *Moskalenko et al.* [1979] have broad CO_2 CIA, which covers the SO_2 absorption band. Since these data show quite different temperature dependence compared to those from recent measurements [*Baranov et al.*, 2004; *Snels et al.*, 2014] (Figure 3b), the broad CIA extending down to 1100 cm^{-1} is doubtful and would require an additional study to confirm it. A further study would be a comparison of different sub-Lorentzian line shape factors in this particular spectral range to make better understanding on thermal flux in this spectral range.

Thermal cooling rate is calculated for the one-dimensional net flux profile, using the following equations,

$$\frac{dT}{dt} = \frac{1}{\rho c_p}\left(-\frac{\partial \mathbf{F}_{net}}{\partial z}\right), \tag{6}$$

where c_p is heat capacity (J kg^{-1} K^{-1}) taken from *Crisp* [1986],

$$c_p(T) = 443.15 + 1.688T - 1.269 \times 10^{-3}T^2 + 3.47 \times 10^{-7}T^3. \tag{7}$$

The results are smoothed over 3 km path length and are compared in Figure 11 considering MIN and MAX trace gas abundances. Since the air density (ρ) increases logarithmically downwards, thermal inertia is very large in the deep atmosphere. Cooling rates therefore become much smaller than those above 60 km altitude [*Lee et al.*, 2015]. Nevertheless, there is a considerable difference between MAX and MIN2 especially above 30 km altitude. Cooling rates may increase by a factor of 2 (or even three for the extreme case MIN).

Our results suggest that the observed abundance variation of trace gases can produce thermal cooling rate change e.g. at 36.5 km from 0.014 K d^{-1} for MAX to 0.029 K d^{-1} for MIN2 (0.077 K d^{-1} for MIN), where d is for Earth day. This is comparable to the meridional gradient of diurnally averaged solar heating rate from 0.011 K d^{-1} at equator to 0.001 K d^{-1} at the pole at 36.1 km altitude [*Tomasko et al.*, 1985]. The ranges of thermal cooling rate variation due to each trace gas abundance are estimated, although this is not shown graphically. That due to the SO_2 abundances is from 0.024 K d^{-1} through 0.026 K d^{-1} to 0.074 K d^{-1} at 36.5 km when the SO_2 abundance varies from 300 ppmv through 80 ppmv to 0 ppmv, respectively (this range of cooling rate variation, 0.05 K d^{-1}, corresponds to 200% of STD cooling rate at the same altitude). That due to the H_2O abundances is from 0.017 K d^{-1} to 0.034 K d^{-1} at the same altitude (68% of STD cooling rate) and that due to the OCS abundances is from 0.020 K d^{-1} to 0.019 K d^{-1} (4% of STD cooling rate), for the maximum and minimum abundances of each trace gas (Table 2), respectively. This confirms that the influence of trace gases should be carefully considered in the net radiative energy balance of the deep atmosphere.

Below the clouds, thermal cooling rates have a very weak latitude dependence, since latitudinal temperature differences are small. Solar heating rates more strongly depend on latitude due to decreasing solar insolation with increasing latitude. A comparison of globally averaged thermal cooling rates and solar heating rates allows to estimate the net radiative energy balance in the lower atmosphere. This is shown in Figure 11 using the global mean solar heating rates given by *Tomasko et al.* [1985]. There is an approximate balance of thermal cooling and solar heating at altitudes below 34 km, while weak cooling dominates between

34 and 40 km. The recent global mean solar heating calculation given by *Haus et al.* [2016] is also shown in Figure 11, using VIRA temperature and cloud opacities according to their Figures 4 and 5. As the authors found a general weak net cooling in the lower atmosphere, our comparison also shows stronger cooling than solar heating. *Lebonnois et al.* [2015] reported similar net cooling results and introduced an additional absorption continuum that can suppress the net cooling. This possibility of insufficient thermal opacity may be caused by not yet known gas absorptions, for example, CO_2 foreign CIA or absorption properties of trace gases in the dense CO_2 atmosphere. In addition, a further study of solar heating rates is required using various cloud opacities, the unknown UV absorber's absorption spectra and abundances, trace gas abundances, and solar irradiance spectra. These results should improve the estimation of the net radiative energy balance in the lower atmosphere.

There are no significant changes in the net thermal flux above ~70 km altitude in all of our sensitivity studies (Figures 9 and 10). This implies that the huge opacity of the clouds can prevent radiative influence from the deep atmosphere on the mesosphere, meaning that any variations will be difficult to be recognized through remote sensing, consistent with a previous study [*Lebonnois et al.*, 2015]. In addition, these various thermal fluxes below the clouds will be absorbed by the clouds and may induce horizontal contrasts of thermal heating rates at the cloud bottom (~48 km). A similar response may also result from lower cloud opacity changes (Figure 7b). This would affect a convective layer in the low-to-middle cloud layers [*Baker et al.*, 1998; *Imamura et al.*, 2014], which has been explored through fluid dynamic model calculations using solar and thermal radiative energies. A further study employing the spatial inhomogeneity of heating at the cloud bottom would be helpful to better our understanding of the convective layer.

5. Summary

We calculated the net thermal fluxes in the atmosphere of Venus from the surface to 100 km altitude. Updated CO_2 collision-induced absorption coefficients (CIA) were included in this study. Compared with values that were measured in the 1970s [*Moskalenko et al.*, 1979], these new data exhibit a considerable discrepancy in the temperature dependence and also in the spectral coverage. Among the updated data sets, we find that the CO_2 CIA in the 2650–3130 cm^{-1} range affects the deep atmospheric thermal flux strongly.

Using the new CIA data, the influence of trace gas abundances on net thermal flux profiles in the lower atmosphere of Venus has been explored in great detail by specifying minimum and maximum abundances of all trace gases reported from observations. Considerable flux variations occur implying the importance of trace gases to understand the net radiative energy balance in the lower atmosphere. The results show that SO_2, H_2O, and OCS are effective thermal opacity sources. The most significant influence may occur when SO_2 abundances would be small (<20 ppmv). H_2O abundance variations from 20 to 40 ppmv also produce considerable changes of the net thermal flux. Various OCS abundances from 0 to 5 ppmv show some effects on the net thermal flux, even though the range of variation is small. CO and HCl abundance variations only weakly modify net thermal fluxes. We also explored the influences of lower clouds and lower haze distribution changes. They turned out to wield little influence on net thermal fluxes below the clouds.

Present results on simulated net flux variations show a successful fitting of in situ measurement data obtained by the decent probes of Pioneer Venus. This means that the observed variations of trace gas abundances facilitate a possible explanation of these measured net flux variations.

Acknowledgments
Supporting data are included as three tables in the supporting information file. Y.J. Lee thanks N. Ignatiev for providing optical properties of cloud aerosols.

References

Allen, D. A., and J. W. Crawford (1984), Cloud structure on the dark side of Venus, *Nature*, *307*, 222–224, doi:10.1038/307222a0.

Arney, G., V. Meadows, D. Crisp, S. J. Schmidt, J. Bailey, and T. Robinson (2014), Spatially resolved measurements of H_2O, HCl, CO, OCS, SO_2, cloud opacity, and acid concentration in the Venus near-infrared spectral windows, *J. Geophys. Res. Planets*, *119*, 1860–1891, doi:10.1002/2014JE004662.

Baker, R. D., G. Schubert, and P. W. Jones (1998), Cloud-level penetrative compressible convection in the Venus atmosphere, *J. Atmos. Sci.*, *55*, 3–18, doi:10.1175/1520-0469(1998)055<0003:CLPCCI>2.0.CO;2.

Baranov, Y. I., W. J. Lafferty, and G. T. Fraser (2004), Infrared spectrum of the continuum and dimer absorption in the vicinity of the O_2 vibrational fundamental in O_2/CO_2 mixtures, *J. Mol. Spectrosc.*, *228*, 432–440, doi:10.1016/j.jms.2004.04.010.

Bertaux, J.-L., T. Widemann, A. Hauchecorne, V. I. Moroz, and A. P. Ekonomov (1996), VEGA 1 and VEGA 2 entry probes: An investigation of local UV absorption (220–400 nm) in the atmosphere of Venus (SO_2, aerosols, cloud structure), *J. Geophys. Res.*, *101*, 12,709–12,746, doi:10.1029/96JE00466.

Bézard, B., C. de Bergh, D. Crisp, and J.-P. Maillard (1990), The deep atmosphere of Venus revealed by high-resolution nightside spectra, *Nature*, *345*, 508–511, doi:10.1038/345508a0.

Bézard, B., C. C. C. Tsang, R. W. Carlson, G. Piccioni, E. Marcq, and P. Drossart (2009), Water vapor abundance near the surface of Venus from Venus Express/VIRTIS observations, *J. Geophys. Res.*, *114*, E00B39, doi:10.1029/2008JE003251.

Bullock, M. A., and D. H. Grinspoon (2001), The recent evolution of climate on Venus, *Icarus*, *150*, 19–37, doi:10.1006/icar.2000.6570.

Clough, S. A., M. W. Shephard, E. J. Mlawer, J. S. Delamere, M. J. Iacono, K. Cady-Pereira, S. Boukabara, and P. D. Brown (2005), Atmospheric radiative transfer modeling: A summary of the AER codes, *J. Quant. Spectrosc. Radiat. Transfer*, *91*, 233–244, doi:10.1016/j.jqsrt.2004.05.058.

Crisp, D. (1986), Radiative forcing of the Venus mesosphere. I—Solar fluxes and heating rates, *Icarus*, *67*, 484–514, doi:10.1016/0019-1035(86)90126-0.

Evans, K. F. (1998), The spherical harmonics discrete ordinate method for three-dimensional atmospheric radiative transfer, *J. Atmos. Sci.*, *55*, 429–446, doi:10.1175/1520-0469(1998)055<0429:TSHDOM>2.0.CO;2.

Eymet, V., R. Fournier, J.-L. Dufresne, S. Lebonnois, F. Hourdin, and M. A. Bullock (2009), Net exchange parameterization of thermal infrared radiative transfer in Venus' atmosphere, *J. Geophys. Res.*, *114*, E11008, doi:10.1029/2008JE003276.

Fedorova, A. et al. (2008), HDO and H_2O vertical distributions and isotopic ratio in the Venus mesosphere by Solar Occultation at Infrared spectrometer on board Venus Express, *J. Geophys. Res.*, *113*, E00B22, doi:10.1029/2008JE003146.

Fegley, B., Jr., and A. H. Treiman (1992), Chemistry of atmosphere-surface interaction on Venus and Mars, in *Venus and Mars: Atmospheres, Ionospheres, and Solar Wind Interactions, Geophys. Monogr. Ser.*, vol. 66, edited by J. G. Luhmann, M. Tatrallyay, and R. O. Pepin, pp. 7–71, AGU, Washington, D. C.

Frommhold, L. (1993), *Collision-Induced Absorption in Gases*, Cambridge Univ. Press, Cambridge, U. K., Cambridge Monogr. on Atomic, Mol. and Chem. Phys.

Gruszka, M., and A. Borysow (1997), Roto-translational collision-induced absorption of CO_2 for the atmosphere of Venus at frequencies from 0 to 250 cm^{-1}, at temperatures from 200 to 800 K, *Icarus*, *129*, 172–177, doi:10.1006/icar.1997.5773.

Halevy, I., R. T. Pierrehumbert, and D. P. Schrag (2009), Radiative transfer in CO_2-rich paleoatmospheres, *J. Geophys. Res.*, *114*, D18112, doi:10.1029/2009JD011915.

Haus, R., D. Kappel, and G. Arnold (2015a), Radiative heating and cooling in the middle and lower atmosphere of Venus and responses to atmospheric and spectroscopic parameter variations, *Planet. Space Sci.*, *117*, 262–294, doi:10.1016/j.pss.2015.06.024.

Haus, R., D. Kappel, and G. Arnold (2015b), Lower atmosphere minor gas abundances as retrieved from Venus Express VIRTIS-M-IR data at 2.3 μm, *Planet. Space Sci.*, *105*, 159–174, doi:10.1016/j.pss.2014.11.020.

Haus, R., D. Kappel, S. Tellmann, G. Arnold, G. Piccioni, P. Drossart, and B. Häusler (2016), Radiative energy balance of Venus based on improved models of the middle and lower atmosphere, *Icarus*, *272*, 178–205, doi:10.1016/j.icarus.2016.02.048.

Hilsenrath, J., C. W. Beckett, W. S. Benedict, L. Fano, H. J. Hoge, J. F. Musi, R. L. Nuttall, and Y. S. Touloukian (1960), *Tables of Thermodynamic and Transport Properties of Air, Argon Carbon Dioxide, Carbon Monoxide, Hydrogen, Nitrogen, Oxygen, and Steam*, Pergamon Press, New York.

Ignatiev, N. I., V. i. Moroz, L. V. Zasova, and I. v. Khatuntsev (1999), Water vapour in the middle atmosphere of Venus: An improved treatment of the Venera 15 IR spectra, *Planet. Space Sci.*, *47*, 1061–1075, doi:10.1016/S0032-0633(99)00030-6.

Ignatiev, N. I., D. V. Titov, G. Piccioni, P. Drossart, W. J. Markiewicz, V. Cottini, T. Roatsch, M. Almeida, and N. Manoel (2009), Altimetry of the Venus cloud tops from the Venus Express observations, *J. Geophys. Res.*, *114*, E00B43, doi:10.1029/2008JE003320.

Imamura, T., T. Higuchi, Y. Maejima, M. Takagi, N. Sugimoto, K. Ikeda, and H. Ando (2014), Inverse insolation dependence of Venus' cloud-level convection, *Icarus*, *228*, 181–188, doi:10.1016/j.icarus.2013.10.012.

Iwagami, N., et al. (2008), Hemispheric distributions of HCl above and below the Venus' clouds by ground-based 1.7 μm spectroscopy, *Planet. Space Sci.*, *56*, 1424–1434, doi:10.1016/j.pss.2008.05.009.

Krasnopolsky, V. A. (2007), Chemical kinetic model for the lower atmosphere of Venus, *Icarus*, *191*, 25–37, doi:10.1016/j.icarus.2007.04.028.

Lebonnois, S., V. Eymet, C. Lee, and J. Vatant d'Ollone (2015), Analysis of the radiative budget of the Venusian atmosphere based on infrared Net Exchange Rate formalism, *J. Geophys. Res. Planets*, *120*, 1186–1200, doi:10.1002/2015JE004794.

Lee, C., and M. I. Richardson (2011), A discrete ordinate, multiple scattering, radiative transfer model of the Venus atmosphere from 0.1 to 260 μm, *J. Atmos. Sci.*, *68*, 1323–1339, doi:10.1175/2011JAS3703.1.

Lee, Y. J., D. V. Titov, N. I. Ignatiev, S. Tellmann, M. Pätzold, and G. Piccioni (2015), The radiative forcing variability caused by the changes of the upper cloud vertical structure in the Venus mesosphere, *Planet. Space Sci.*, *113*, 298–308, doi:10.1016/j.pss.2014.12.006.

Marcq, E., B. Bézard, T. Encrenaz, and M. Birlan (2005), Latitudinal variations of CO and OCS in the lower atmosphere of Venus from near-infrared nightside spectro-imaging, *Icarus*, *179*, 375–386, doi:10.1016/j.icarus.2005.06.018.

Marcq, E., T. Encrenaz, B. Bézard, and M. Birlan (2006), Remote sensing of Venus' lower atmosphere from ground-based IR spectroscopy: Latitudinal and vertical distribution of minor species, *Planet. Space Sci.*, *54*, 1360–1370, doi:10.1016/j.pss.2006.04.024.

Marcq, E., B. Bézard, P. Drossart, G. Piccioni, J. M. Reess, and F. Henry (2008), A latitudinal survey of CO, OCS, H_2O, and SO_2 in the lower atmosphere of Venus: Spectroscopic studies using VIRTIS-H, *J. Geophys. Res.*, *113*, E00B07, doi:10.1029/2008JE003074.

Marov, M. Y. (1978), Results of Venus missions, *Annu. Rev. Astron. Astrophys.*, *16*, 141–169, doi:10.1146/annurev.aa.16.090178.001041.

Meadows, V. S., and D. Crisp (1996), Ground-based near-infrared observations of the Venus nightside: The thermal structure and water abundance near the surface, *J. Geophys. Res.*, *101*, 4595–4622, doi:10.1029/95JE03567.

Mendonça, J. M., P. L. Read, C. F. Wilson, and C. Lee (2015), A new, fast and flexible radiative transfer method for Venus general circulation models, *Planet. Space Sci.*, *105*, 80–93, doi:10.1016/j.pss.2014.11.008.

Moroz, V. I., A. P. Ekonomov, B. E. Moshkin, H. E. Revercomb, L. A. Sromovsky, and J. T. Schofield (1985), Solar and thermal radiation in the Venus atmosphere, *Adv. Space Res.*, *5*, 197–232, doi:10.1016/0273-1177(85)90202-9.

Moskalenko, N. I., I. A. Ilin, S. N. Parzhin, and L. V. Rodionov (1979), Pressure-induced infrared radiation absorption in atmospheres, *Atmos. Oceanic Phys.*, *15*(9), 632–637.

Oyama, V. I., G. C. Carle, F. Woeller, J. B. Pollack, R. T. Reynolds, and R. A. Craig (1980), Pioneer Venus gas chromatography of the lower atmosphere of Venus, *J. Geophys. Res.*, *85*, 7891–7902, doi:10.1029/JA085iA13p07891.

Palmer, K. F., and D. Williams (1975), Optical constants of sulfuric acid—Application to the clouds of Venus, *Appl. Opt.*, *14*, 208–219.

Piccioni, G., et al. (2006), *VIRTIS: The Visible and Infrared Thermal Imaging Spectrometer*, vol. SP-1295, ESA, Noordwijk, Netherlands.

Pollack, J. B., O. B. Toon, R. C. Whitten, R. Boese, B. Ragent, M. Tomasko, L. Eposito, L. Travis, and D. Wiedman (1980a), Distribution and source of the UV absorption in Venus' atmosphere, *J. Geophys. Res.*, *85*, 8141–8150, doi:10.1029/JA085iA13p08141.

Pollack, J. B., O. B. Toon, and R. Boese (1980b), Greenhouse models of Venus' high surface temperature, as constrained by Pioneer Venus measurement, *J. Geophys. Res.*, *85*, 8223–8231, doi:10.1029/JA085iA13p08223.

Pollack, J. B., et al. (1993), Near-infrared light from Venus' nightside—A spectroscopic analysis, *Icarus*, *103*, 1–42, doi:10.1006/icar.1993.1055.

Ptashnik, I. V., R. A. McPheat, K. P. Shine, K. M. Smith, and R. G. Williams (2011), Water vapor self-continuum absorption in near-infrared windows derived from laboratory measurements, *J. Geophys. Res.*, *116*, D16305, doi:10.1029/2011JD015603.

Ptashnik, I. V., R. A. McPheat, K. P. Shine, K. M. Smith, and R. G. Williams (2012), Water vapour foreign-continuum absorption in near-infrared windows from laboratory measurements, *Philos. Trans. R. Soc. A.*, *370*(1968), 2557–2577, doi:10.1098/rsta.2011.0218.

Ptashnik, I. V., T. M. Petrova, Y. N. Ponomarev, K. P. Shine, A. A. Solodov, and A. M. Solodov (2013), Near-infrared water vapour self-continuum at close to room temperature, *J. Quant. Spectrosc. Radiat. Transfer*, *120*, 23–35, doi:10.1016/j.jqsrt.2013.02.016.

Revercomb, H. E., L. A. Sromovsky, and V. E. Suomi (1982), Reassessment of net radiation measurements in the atmosphere of Venus, *Icarus*, *52*, 279–300, doi:10.1016/0019-1035(82)90113-0.

Revercomb, H. E., L. A. Sromovsky, V. E. Suomi, and R. W. Boese (1985), Net thermal radiation in the atmosphere of Venus, *Icarus*, *61*, 521–538, doi:10.1016/0019-1035(85)90140-X.

Rothman, L. S., I. E. Gordon, R. J. Barber, H. Dothe, R. R. Gamache, A. Goldman, V. I. Perevalov, S. A. Tashkun, and J. Tennyson (2010), HITEMP, the high-temperature molecular spectroscopic database, *J. Quant. Spectrosc. Radiat. Transfer*, *111*, 2139–2150, doi:10.1016/j.jqsrt.2010.05.001.

Rothman, L. S., et al. (2013), The HITRAN2012 molecular spectroscopic database, *J. Quant. Spectrosc. Radiat. Transfer*, *130*, 4–50, doi:10.1016/j.jqsrt.2013.07.002.

Schofield, J. T., and F. W. Taylor (1982), Net global thermal emission from the Venusian atmosphere, *Icarus*, *52*, 245–262, doi:10.1016/0019-1035(82)90111-7.

Seiff, A., J. T. Schofield, A. J. Kliore, F. W. Taylor, and S. S. Limaye (1985), Models of the structure of the atmosphere of Venus from the surface to 100 kilometers altitude, *Adv. Space Res.*, *5*, 3–58, doi:10.1016/0273-1177(85)90197-8.

Shillings, A. J. L., S. M. Ball, M. J. Barber, J. Tennyson, and R. L. Jones (2011), An upper limit for water dimer absorption in the 750 nm spectral region and a revised water line list, *Atmos. Chem. Phys.*, *11*, 4273–4287, doi:10.5194/acp-11-4273-2011.

Snels, M., S. Stefani, D. Grassi, G. Piccioni, and A. Adriani (2014), Carbon dioxide opacity of the Venus' atmosphere, *Planet. Space Sci.*, *103*, 347–354, doi:10.1016/j.pss.2014.08.002.

Stefani, S., G. Piccioni, M. Snels, D. Grassi, and A. Adriani (2013), Experimental CO_2 absorption coefficients at high pressure and high temperature, *J. Quant. Spectrosc. Radiat. Transfer*, *117*, 21–28, doi:10.1016/j.jqsrt.2012.11.019.

Suomi, V. E., L. A. Sromovsky, and H. E. Revercomb (1980), Net radiation in the atmosphere of Venus: Measurements and interpretation, *J. Geophys. Res.*, *85*(A13), 8200–8218, doi:10.1029/JA085iA13p08200.

Takagi, M., K. Suzuki, H. Sagawa, P. Baron, J. Mendrok, Y. Kasai, and Y. Matsuda (2010), Influence of CO_2 line profiles on radiative and radiative-convective equilibrium states of the Venus lower atmosphere, *J. Geophys. Res.*, *115*, E06014, doi:10.1029/2009JE003488.

Taylor, F., and D. Grinspoon (2009), Climate evolution of Venus, *J. Geophys. Res.*, *114*, E00B40, doi:10.1029/2008JE003316.

Taylor, F. W. (2006), Venus before Venus Express, *Planet. Space Sci.*, *54*, 1249–1262, doi:10.1016/j.pss.2006.04.031.

Thomas, M. E., and M. J. Linevsky (1989), Integrated intensities of N_2, CO_2, and SF_6 vibrational bands from 1800 to 5000 cm^{-1} as a function of density and temperature, *J. Quant. Spectrosc. Radiat. Transfer*, *42*, 465–476, doi:10.1016/0022-4073(89)90037-X.

Titov, D. V., and R. Haus (1997), A fast and accurate method of calculation of gaseous transmission functions in planetary atmospheres, *Planet. Space Sci.*, *45*, 369–377, doi:10.1016/S0032-0633(96)00129-8.

Titov, D. V., M. A. Bullock, D. Crisp, N. O. Renno, F. W. Taylor, and L. V. Zasova (2007), Radiation in the atmosphere of Venus, in *Exploring Venus as a Terrestrial Planet*, edited by L. Esposito, E. R. Stofan, and T. E. Cravens, pp. 121–138, AGU, Washington, D. C.Geophysical. Monogr. Ser.

Tomasko, M. G. (1983), The thermal balance of the lower atmosphere of Venus, in *Venus*, edited by D. M. Hunten et al., pp. 604–631, Univ. of Arizona Press, Tucson, Ariz.

Tomasko, M. G., L. R. Doose, and P. H. Smith (1985), The absorption of solar energy and the heating rate in the atmosphere of Venus, *Adv. Space Res.*, *5*, 71–79, doi:10.1016/0273-1177(85)90272-8.

Tonkov, M. V., N. N. Filippov, V. V. Bertsev, J. P. Bouanich, N. van-Thanh, C. Brodbeck, J. M. Hartmann, C. Boulet, F. Thibault, and R. Le Doucen (1996), Measurements and empirical modeling of pure CO_2 absorption in the 2.3-μm region at room temperature: Far wings, allowed and collision-induced bands, *Appl. Opt.*, *35*, 4863–4870, doi:10.1364/AO.35.004863.

Tsang, C. C. C., F. W. Taylor, C. F. Wilson, S. J. Liddell, P. G. J. Irwin, G. Piccioni, P. Drossart, and S. B. Calcutt (2009), Variability of CO concentrations in the Venus troposphere from Venus Express/VIRTIS using a Band Ratio Technique, *Icarus*, *201*, 432–443, doi:10.1016/j.icarus.2009.01.001.

von Zahn, U., S. Kumar, H. Niemann, and R. Prinn (1983), Composition of the Venus atmosphere, in *Venus*, edited by D. M. Hunten et al., pp. 299–430, Univ. of Arizona Press, Tucson, Ariz.

Wattson, R., and L. Rothman (1992), Direct numerical diagonalization: Wave of the future, *J. Quant. Spectrosc. Radiat. Transfer*, *48*, 763–780, doi:10.1016/0022-4073(92)90140-Y.

Winters, B., S. Silverman, and W. S. Benedict (1964), Line shape in the wing beyond the band head of the 4.3 μ band of CO_2, *J. Quant. Spectrosc. Radiat. Transfer*, *4*, 527–537, doi:10.1016/0022-4073(64)90014-7.

Wiscombe, W. J. (1980), Improved Mie scattering algorithms, *Appl. Opt.*, *19*, 1505–1509, doi:10.1364/AO.19.001505.

Zasova, L. V., N. Ignatiev, I. Khatuntsev, and V. Linkin (2007), Structure of the Venus atmosphere, *Planet. Space Sci.*, *55*, 1712–1728, doi:10.1016/j.pss.2007.01.011.